

TRAILING VORTEX MEASUREMENTS IN THE WAKE OF A HOVERING ROTOR BLADE WITH VARIOUS TIP SHAPES

Preston B. Martin *

pbmartin@mail.arc.nasa.gov

U.S. Army Aeroflightdynamics Directorate (AMCOM)

Army/NASA Rotorcraft Division

Ames Research Center M/S 215-1

Moffett Field, CA 95008

J. Gordon Leishman**

leishman@eng.umd.edu

Alfred Gessow Rotorcraft Center

Department of Aerospace Engineering

Glenn L. Martin Institute of Technology

University of Maryland, College Park, Maryland 20742

Abstract

This work examined the wake aerodynamics of a single helicopter rotor blade with several tip shapes operating on a hover test stand. Velocity field measurements were conducted using three-component laser Doppler velocimetry (LDV). The objective of these measurements was to document the vortex velocity profiles and then extract the core properties, such as the core radius, peak swirl velocity, and axial velocity. The measured test cases covered a wide range of wake-ages and several tip shapes, including rectangular, tapered, swept, and a subwing tip. One of the primary differences shown by the change in tip shape was the wake geometry. The effect of blade taper reduced the initial peak swirl velocity by a significant fraction. It appears that this is accomplished by decreasing the vortex strength for a given blade loading. The subwing measurements showed that the interaction and merging of the subwing and primary vortices created a less coherent vortical structure. A source of vortex core instability is shown to be the ratio of the peak swirl velocity to the axial velocity deficit. The results show that if there is a turbulence producing

region of the vortex structure, it will be outside of the core boundary. The LDV measurements were supported by laser light-sheet flow visualization. The results provide several benchmark test cases for future validation of theoretical vortex models, numerical free-wake models, and computational fluid dynamics results.

Nomenclature

A	rotor disk area = πR^2 , m^2
BEMT	blade element momentum theory
C_T	rotor thrust coefficient = $T/\rho A (\Omega R)^2$
C_θ	Ludwig vortex stability swirl coefficient
C_z	Ludwig vortex stability axial coefficient
c	rotor blade chord, m
f	Gudermannian function
k_1	ratio = Γ_v/Γ_b
k_2	ratio = $(\Gamma_b/\Omega R c)/(C_T/\sigma)$
l	mixing length
N_b	number of blades
r	radial distance from vortex core center, m
r_c	vortex viscous core radius, m
R	rotor blade radius, m
Re	Reynolds number
Re_v	vortex Reynolds number = Γ_v/ν
Ri	Richardson number
R_L	re-laminarization parameter
R_{Lc}	re-laminarization parameter at $r = r_c$
S	Leibovich-Stewartson vortex stability param.

* Research Engineer.

Formerly: Graduate Research Assistant, Univ. of Maryland,

** Professor.

Presented at the 58th Annual Forum of the AHS International, Montréal Canada, June 11–13, 2002. ©2002 by the authors.

Published by the American Helicopter Society International with permission

S_p	Bradshaw's shape parameter
t_0	effective time offset based on r_c at $t = 0$, sec
t	time, sec
T	rotor thrust, N
TPP	tip path plane
V_{ax}	axial velocity deficit in the vortex core, m/s
V_θ	vortex tangential (swirl) velocity, m/s
y	dimensional radial distance along blade, m
z	vertical distance from TPP, m
α	Iverson's empirical constant = 0.01854
η	similarity variable = $r^2 / (4\alpha^2 \Gamma_v \tau)$
γ	vortex circulation profile, Γ / Γ_v
γ_{tr}	transitional vortex circulation profile
Γ	local vortex circulation, m^2/s
Γ_b	peak bound circulation, m^2/s
Γ_v	total vortex circulation, m^2/s
Γ_c	vortex core circulation = $2\pi V_{\theta_{max}} r_c$, m^2/s
λ	mean inflow velocity ratio through the TPP
ν	kinematic viscosity, m^2/s
ν_T	effective turbulent viscosity, m^2/s
Ω	angular velocity of rotor blade, rad/s
ρ	air density, kg/m^3
σ	rotor solidity = $N_b c / \pi R$
τ	time variable = $t + t_0$
ζ	wake age of vortex core from TE, deg

Introduction

Many experiments have been attempted to examine the formation of lift-generated tip vortices. Two of the most detailed surveys are given by Rossow (Ref. 1) and Spalart (Ref. 2). Some of the first phase-resolved measurements of helicopter rotor flow fields were attempted using hot-wire anemometry (e.g., Refs. 3–8). Modern optical flow diagnostic techniques, such as laser Doppler velocimetry (LDV) and particle image velocimetry (PIV), can alleviate many of the limitations of hot-wire anemometry. An early application of a one-component LDV system to a rotor flow field was by Landgrebe & Johnson (Ref. 9), who provided a demonstration of its potential capabilities. Another application was that of Lorber et al. (Ref. 10) using 2D LDV to measure the circulation field around the blade of a Mach-scaled UH-60A with surface-mounted pressure transducers.

Over the last thirty years, LDV has gradually matured to allow simultaneous three-component flow field measurements with excellent spatial and temporal resolution (e.g., Refs. 11–15). Recently, PIV has become a rapidly maturing and competitive technique, as shown by the measurements of Heineck et al. (Ref. 16) and McAlister et al. (Ref. 17). A summary of the relative capabilities

and limitations of the LDV and PIV techniques, as they apply to the measurement of rotor vortex flows, is given by Martin et al. (Ref. 18). The current work builds on the measurements reported by Leishman and co-workers (Refs. 15, 19–21).

Results of detailed flow visualization (Refs. 22 and 23) have documented the viscous flow field surrounding the rotor blade tip. The physical size of these vortical flow structures is only a fraction of the blade thickness, and so a fine level of spatial resolution is required to capture and resolve details of the vortex core. A fine level of temporal resolution (i.e., phase resolution) is required by the dynamic nature of the interaction and convection of the vortex filaments. These resolution requirements are critical when comparing different tip shapes.

The present work involves three-dimensional velocity measurements acquired in the flow field surrounding the tip of a one-bladed rotor in hover. An analysis of the measurement uncertainties involved in making these types of measurements using laser Doppler velocimetry (LDV) is described in Ref. 24. As a result of this initial study, the LDV technique was significantly refined and enabled the measurements presented here. Examples of the preliminary and refined techniques are given for several of the test cases. The results are from Refs. 25 and 26, and are compared to the baseline test case presented in Ref. 23.

Phase-resolved LDV measurements documenting the formation, roll-up, and evolution of the blade tip vortex were acquired by making a radial traverse across the vortex core at various planes below the rotor. This allowed the core properties to be studied as a function of wake age. The measurements for three other tip shapes were compared with the baseline blade. The planforms included a 20° swept tip, a tapered tip with a 0.4 taper ratio, and a subwing tip. The vortex properties estimated from the velocity profiles were compared to the baseline measurements.

Physical Description of a Rotor Wake

The combined wake of a hovering rotor can be visualized as a system of interacting helical surfaces of vorticity (vortex sheets) and discrete tip vortices imposed within a streamtube of actuated fluid. It is the rotational motion of the rotor blade about the shaft that causes the spanwise lift distribution on the blade to be biased outboard, toward the tip. A representative lift distribution is shown in Fig. 1. As a result, a strong static pressure gradient forms around the tip region, and the outboard portion of the wake surface experiences a roll-up into an

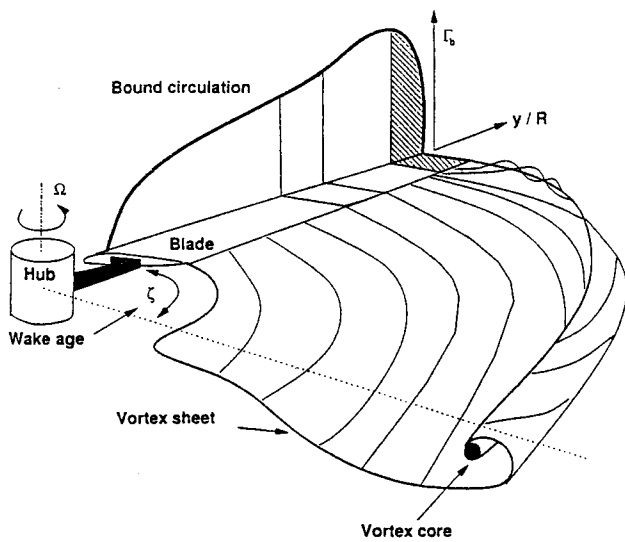


Figure 1: Schematic showing the bound circulation distribution and the corresponding trailing wake on a rotor blade.

intense region of vorticity in the form of a trailing tip vortex. The near-field tip vortex aerodynamics involve the confluence of the trailing edge turbulent wake and any edge-separated flow into a viscous vortex core. As will be shown, this process is a function of tip shape.

Figure 1 shows that a fixed azimuthal distance from the blade trailing edge is defined as the wake age, ζ . This figure also shows the qualitative relationship between the bound circulation distribution on the blade and the trailing wake structure. For a multi-bladed rotor in hover, the details of the trailing wakes are shown by Fig. 2 in an axial/radial plane at a fixed value of wake age, ζ . It is evident that the wake generated by a helicopter rotor is characterized by highly dynamic, interacting vortical flow structures (e.g., Ref. 27).

In contrast to a fixed wing aircraft, the rotor tip vortices remain close to the blades. This is especially true under certain flight conditions such as low-speed descending flight, and during transition to forward flight. Not only does the wake interact with the main rotor blades, but the filaments may intersect the tail rotor, the vertical and horizontal stabilizers, and the airframe. Even in hover, the vortices pass within a fraction of a chord length below the following blades. This small blade/vortex miss distance results in high induced velocities including both upwash and downwash components, as well as radial flow. The velocity gradients induced by an individual blade's trailing vortex has been shown to cause stall on the tip of the following blade – see Clark and Leiper (Ref. 28). The magnitude and direction of these induced velocities depends on the vortex strength, the distance from the blade, and the orientation of the

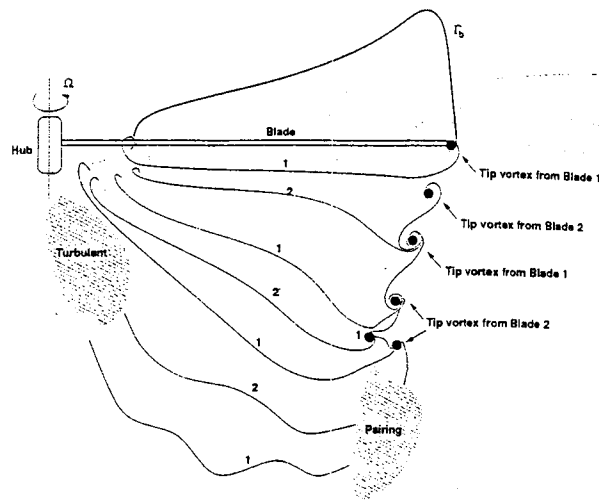


Figure 2: Schematic showing a cross-section of the wake of a two-bladed rotor operating in hover.

filament with respect to the blade. A primary example of this is shown by the measurements of Berenger et al. (Ref. 29).

The proximity of the wake to the rotor in hover creates a condition where small perturbations of the rotor inflow can cause the vortices to remain in the plane of the rotor during descending flight, in transition to forward flight, and during transient gusts. As will be shown by this fundamental set of experiments, the effects of both swept and tapered tips are to keep the vortices closer to the TPP than for a rectangular tip in hover.

As a direct result of the vortices remaining near the TPP, substantial unsteady variations in the local induced velocity field are then encountered by the rotating blades. Blade-vortex interaction (BVI) manifests as a rapidly fluctuating angle of attack that results in an unsteady local blade loading. One key to predicting the magnitude of these angle of attack variations is to develop a better understanding of the vortex core structure (see Ref. 26). It is the coupling of the wake induced velocities to the rotor blade dynamics that makes understanding the wake physics important for steady flight predictions, and critical for maneuvering flight predictions and/or simulations.

Experimental Apparatus

Rotor Test Stand

The planforms tested in these experiments included a 20° swept tip (sheared), tapered tip with a 0.4 taper ratio, and a subwing tip. The blade parameters and test conditions are given in the Appendix. The rotors were tested in the hovering state in a specially designed flow

conditioned test cell. The volume of the test cell was approximately 12,800 ft³ (362 m³) and was surrounded by honeycomb screens. This cell was located inside a large 500,000 ft³ (14,000 m³) high-bay laboratory. The rotor disk area was 5.6 ft² (0.52 m²), and the wake was allowed to exhaust approximately 18 rotor radii before encountering flow diverters. Aperiodicity levels in the rotor wake when tested in this cell have been measured and used to correct the velocity field measurements (see Ref. 26).

LDV System

A fiber-optic based LDV system was used to make three-component velocity measurements. A beam splitter separated a single multi-line Argon-Ion laser beam into three pairs of beams (green, blue and violet), each of which measured a single component of velocity (see Fig. 3). A Bragg cell set to a frequency shift of 40 MHz produced the second shifted beam of each beam pair.

The laser beams were passed to the transmitting optics by a set of fiber-optic couplers with single mode polarization preserving fiber optic cables. The transmitting optics were located adjacent to the rotor, and consisted of a pair of fiber optic probes with integral receiving optics, one probe for the green and blue pairs, and the other probe for the violet pair. Beam expanders with focusing lenses of 750 mm and beam spacers were used to decrease the effective size of the measurement volume.

To further reduce the effective size of the probe volume visible to the receiving optics, the off-axis backscatter technique was used, as described in Martin et al. (Ref. 24) and Barrett & Swales (Ref. 32). This technique spatially filters the effective length of the LDV probe volume on all three channels. Spatial coincidence of the three probe volumes (six beams) and two receiving fibers was ensured to within a 25 μ m radius using an alignment technique based on a laser beam profiler, as described in Ref. 24. Alignment is critical for 3-component systems because it is geometric coincidence that determines the spatial resolution of the LDV probe volume. In the present case, the resulting LDV probe volume was measured to be an ellipsoid of dimensions 80 μ m by 150 μ m, which was about 3% of the maximum blade thickness (or about 0.5% of the blade chord).

The flow into the rotor was seeded with a thermally produced mineral oil fog. A mineral oil based fluid is broken down into a fine mist by adding nitrogen. The mist is then forced into a pressurized heater block and heated to its boiling point where it becomes vaporized. As the vapor escapes from the heat exchanger nozzle it is mixed with ambient air, rapidly cools, and condenses into a fog of which 95% of the particles are between 0.2 μ m and 0.22 μ m in diameter. This mean seed parti-

cle size is small enough to minimize particle tracking errors for the vortex strengths found in these experiments (Ref. 33). The fog/air mixture was passed through a series of ventilation ducts and introduced into the rotor flow field at various locations. The entire test area was uniformly seeded by running the fog generator before each measurement. The 30,000 ft³ (850 m³) per minute capacity of the seeder allowed the entire test cell to be uniformly seeded in approximately 30 seconds.

Signal bursts from seed particles passing through the measurement volume were received by the optics, and transmitted to a set of photomultiplier tubes where they were converted to analog signals. This analog signal was bandpass filtered from 10MHz–100MHz to remove the signal pedestal and any high frequency noise. The large range of the bandpass filter was required to allow measurement of the large flow reversal associated with the convection of a vortex core and the blade passage. The analog signal was digitized and sampled using a digital burst correlator. The flow velocities were then converted into three orthogonal components based on measurements of the beam crossing angles. Each measurement was phase-resolved with respect to the rotating blade by using a rotary encoder, which tagged each data point with a time stamp. The temporal phase-resolution of the encoder was 0.1°; however, the measurements were averaged into one-degree bins. The measurement uncertainty in using a one-degree bin width has been discussed by Martin et al. (Ref. 24).

Results and Discussion: Tip Shape Effects

Phase-resolved LDV measurements documenting the formation, roll-up, and evolution of the blade tip vortex were acquired by making a radial traverse across the vortex core at various planes below the rotor. This allowed the core properties to be studied as a function of wake age, ζ , (see Fig. 4). The measurements for three other tip shapes were compared with the baseline blade. The planforms included a 20° swept back tip, a tapered tip with a 0.4 taper ratio, and a subwing tip. The vortex properties estimated from the velocity profiles were compared to the baseline measurements. In addition to the comparison, each of these test cases can be used for validating the ability of aerodynamic models to represent the effects of tip shape on the wake geometry and vortex properties.

Baseline Blade Vortex Properties

The vortex measurements for the baseline blade are reproduced for comparison from Ref. 23. Figure 4 shows

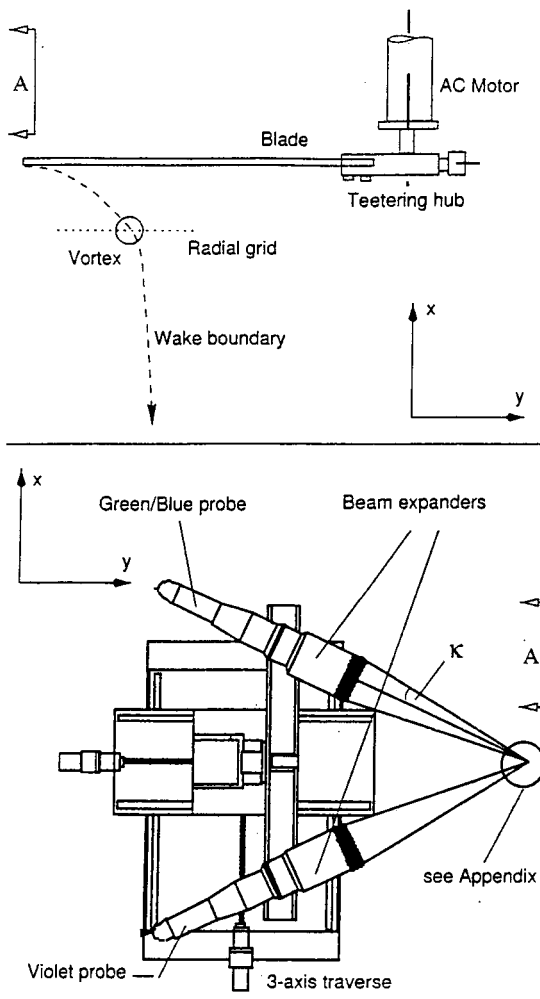


Figure 3: Rotor test stand and LDV system.

the measured wake geometry. Figure 5 shows the variation of the vortex core radius with wake age, and Fig. 6 shows the variation of peak swirl velocity. In both of these figures, the aperiodicity corrections (based on light sheet measurements of core position) are also compared to the uncorrected measurements.

Wake Geometry

The test case parameters for the swept and tapered tip blades are shown in Tables A2 and A3, respectively. In both cases, the blade was of constant chord from the root cut-out at 20% radius to the break-point at 80% radius. Estimates of the bound circulation distribution are shown in Fig. 7(a) using blade element momentum theory (BEMT) (Ref. 41). For comparison, the phase-averaged inflow measurements are shown across the TPP in Fig. 7(b). Note that without a force balance, the peak bound circulation (and therefore the tip vortex

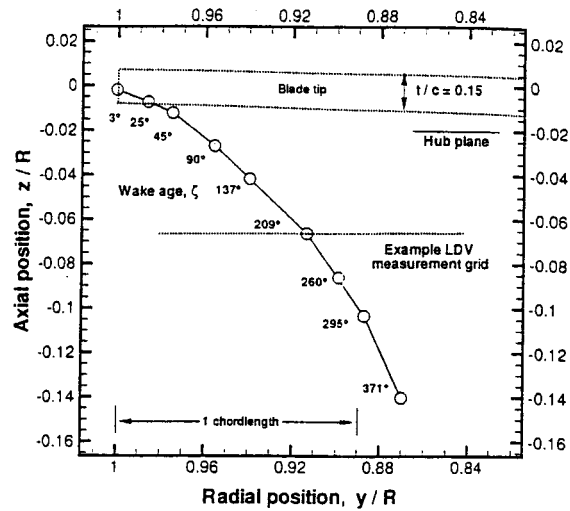


Figure 4: Schematic showing measured wake geometry.

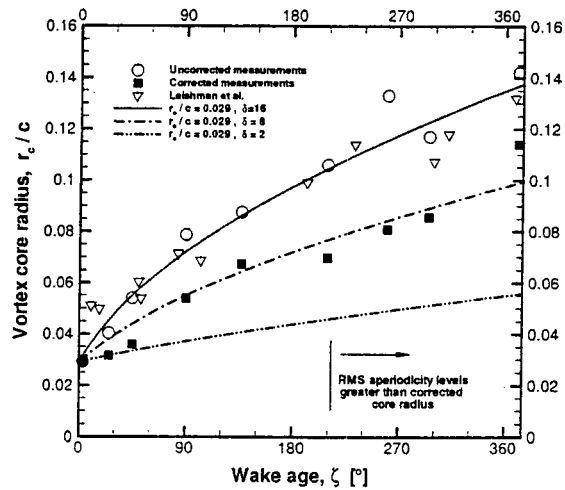


Figure 5: Vortex core radius (inferred from velocity profiles) as a function of wake age for the baseline blade.

strength) could not be matched exactly. Even so, each of these test cases provides a useful set of measurements to compare with numerical predictions.

One of the primary differences shown by the change in tip shape was the measured wake geometry shown in Fig. 8. The primary effect of taper is to decrease the bound circulation near the tip [see Fig. 7(a)], and this also decreases the effective downwash behind the blade [see Fig. 7(b)]. As a result, the vortex tends to stay near the TPP for a larger fraction of a rotor revolution while moving radially inward at a much faster rate, as shown in Fig. 8. The primary effect of sweep appears to be that

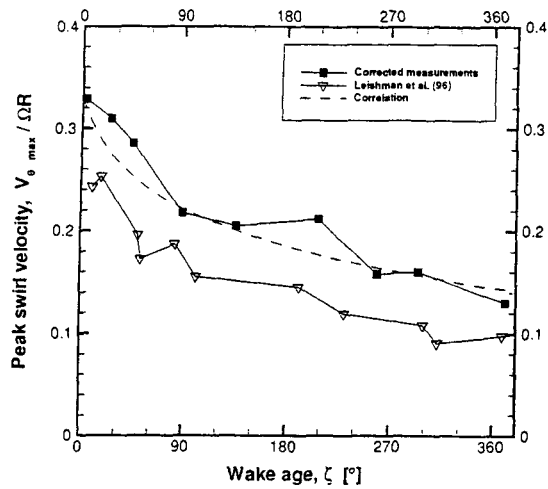


Figure 6: Vortex peak swirl velocity as a function of wake age for the baseline blade.

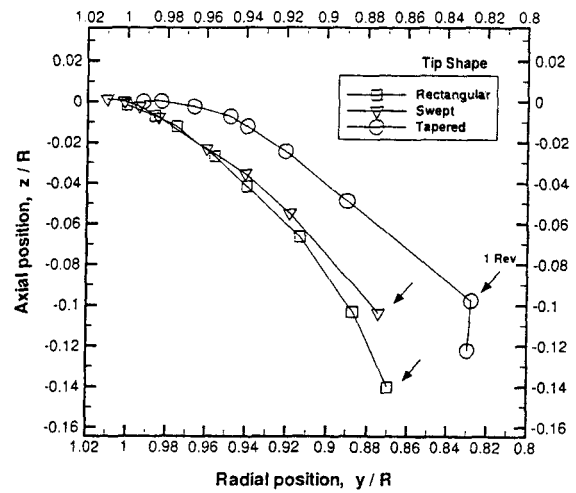


Figure 8: Measured wake geometry for different tip shapes.

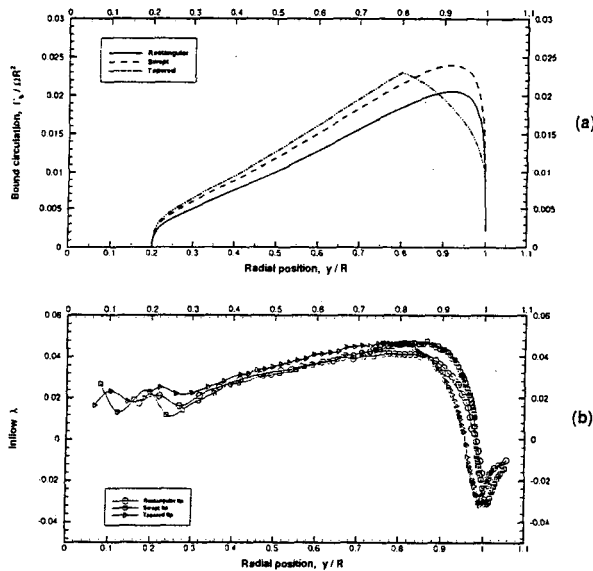


Figure 7: (a) Bound circulation distribution predicted using BEMT, (b) Measured phase-average inflow distribution.

the vortex core is trailed outboard of the 100% radial station. The reason for this is shown by a top view in Fig. 9, where the outer edge of the swept tip does not conform to the circular streamlines. This tip shape is actually a “sheared” tip, with the airfoil chordlines perpendicular to the unswept line of aerodynamic centers (as opposed to the swept line of aerodynamic centers for true sweep). The final result is that sweep appears to decrease both the radial and axial convection of the vortex core, while

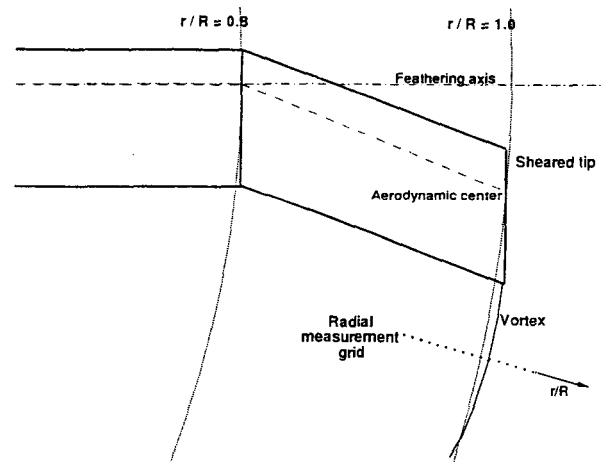


Figure 9: Effect of swept tip in moving the initial core outside of $r/R = 1$.

taper appears to increase the radial convection and decrease the axial convection.

Vortex Core Properties

The comparison of different tip shapes using vortex velocity field measurements requires great care in the experimental methods. Preliminary measurements were used to identify the locations of the vortices and to understand issues related to measurement uncertainty and spatial resolution. The variation of the vortex core radius (estimated from the velocity measurements) is shown in Figs. 10 and 11 as a function of wake age for the preliminary measurements and also for the refined measure-

ment technique, respectively. Over the first quarter of a rotor revolution, the vortex core size is on the order of the boundary layer thickness leaving the trailing edge for each of the blades. The error in the preliminary measurements over this region is significant when compared to the refined technique. In addition, clear trends and vortex structure are difficult to define in the presence of large measurement scatter. It is also important to note that as the spatial resolution degrades at early wake age, the variation in core radius with wake age appears constant.

There is little difference in the vortex core growth shown in Figure 10 between the various tip shapes. As a result, the baseline aperiodicity measurements in Fig. 5 are assumed to be a good approximation for the other tip shapes – with the exception of the subwing tip. In terms of the peak swirl velocity, differences appear for the various tip shapes. A comparison is shown in Fig. 12, where the effects of blade loading variation between the cases have been removed to a first order by normalizing the peak swirl velocity by the average lift coefficient. The reason for this normalization is that the main focus of tip shape modification for BVI reduction is to minimize the peak swirl velocity for a given blade loading.

The vortex peak swirl velocity (divided by tip speed) is a function of three factors, and these are the nondimensional vortex strength, the ratio of core circulation to the far-field value, and the nondimensional vortex core radius.

$$\frac{V_{\theta_{max}}}{\Omega R} = \left(\frac{\Gamma_v}{\Omega R c} \right) \left(\frac{\Gamma_c}{\Gamma_v} \right) \left(\frac{c}{2\pi r_c} \right) \quad (1)$$

The vortex strength is directly proportional to the peak bound circulation, and this is the strongest influence on peak swirl velocity.

$$\frac{V_{\theta_{max}}}{\Omega R} = \left(k_1 \frac{\Gamma_b}{\Omega R c} \right) \left(\frac{\Gamma_c}{\Gamma_v} \right) \left(\frac{c}{2\pi r_c} \right) \quad (2)$$

where k_1 is the ratio of the vortex strength to the peak bound circulation

$$k_1 = \frac{\Gamma_v}{\Gamma_b} \quad (3)$$

Typical values appear to be $k_1 = 1$ for an untwisted blade, and $k_1 = 0.7$ for a highly twisted (tiltrotor) blade, but this needs additional research. The peak bound circulation is a function of blade planform (twist, taper, and sweep) and blade loading.

$$\frac{V_{\theta_{max}}}{\Omega R} = \left(\frac{C_T}{\sigma} \right) (k_1 k_2) \left(\frac{\Gamma_c}{\Gamma_v} \right) \left(\frac{c}{2\pi r_c} \right) \quad (4)$$

where the proportionality constant, k_2 , is defined by

$$\left(\frac{\Gamma_b}{\Omega R c} \right) = k_2 \left(\frac{C_T}{\sigma} \right) \quad (5)$$

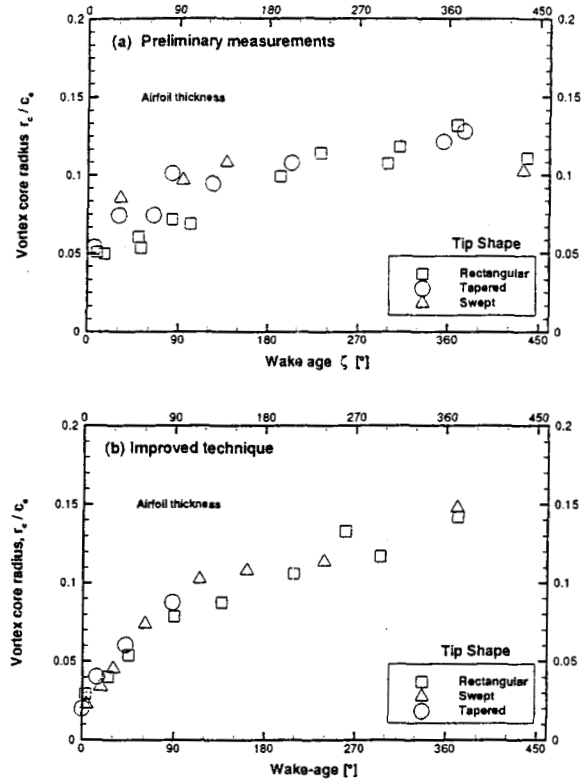


Figure 10: Variation of vortex core radius (uncorrected) with wake-age (a) Preliminary measurements (b) Measurements using improved technique.

Typical values for k_2 in hover are 2 for an ideally twisted rectangular blade and 3 for an untwisted rectangular blade.

The primary influence of tip shape is found in the last three terms of Eq. 4. By dividing the peak swirl velocity by the factor $6C_T/\sigma$ (average lift coefficient), the first term of Eq. 4 is removed. This allows the comparison of the tip shapes to avoid the influence of slightly different values of blade loading. This is shown by comparing the results in Figs. 11 and 12.

A primary example of this reasoning is shown by the tapered tip blade. The estimated peak bound circulation for both the swept and tapered tips is approximately equal (see Fig. 7); however, the blade loading of the tapered tip is slightly higher. As a result, the tapered tip blade reduces the initial peak swirl velocity by reducing the peak bound circulation (i.e., reducing k_2) for a given blade loading. This benefit appears to decrease with wake age. It is interesting to note that once the difference in blade loading is accounted for, the swept and baseline blades show similar behavior.

Subwing Blade

The subwing blade concept has been investigated in wind tunnels (such as part of the NASA XV-15 test program in Ref. 30) as well as in flight tests. A detailed survey of subwing rotor blade tests is given by Ref. 25. In this current test, the subwing blade was constructed starting with a normal rectangular blade. Based on the results of Tangler (Ref. 31), the subwing chord was designed to be about 20% of the main blade chord and was placed at the quarter-chord position on the blade. The profile of the subwing was a flat plate set at a pitch angle the same as that of the main blade. Manufacturing constraints resulted in a subwing tip having a chord of 19.3% of the main blade chord, with the quarter-chord of the subwing being aligned with the 26.4% chord position on the main blade. The operating parameters for the subwing experiments are shown in Table A4, and were meant to be nominally the same as those used for the baseline experiments. As the subwing added less than 1% to the total blade area, its addition was assumed to cause no difference in the geometric or thrust-weighted rotor solidities. A single teetering blade was used and was balanced by a counterweight.

As with the other blades, the phase-averaged inflow was used to provide an estimate of the thrust coefficient of the rotor. The inflow was measured across the TPP, as shown in Fig. 13. Based on these results, BEMT was used numerically to find a rotor thrust coefficient of 0.0033. Using the blade solidity, the blade loading coefficient was then determined to be 0.0959. This is significantly higher than that found for the baseline blade, and was unexpected because of the nearly identical operating conditions (blade pitch and RPM). The exact cause of this dissimilarity is not currently understood; however, changes in performance caused by the subwing design have been documented by several other tests (these are summarized in Ref. 25). One possible reason is that the subwing reduces the tip loss of the main blade as evidenced by the difference in the phase-averaged inflow near the tip.

Subwing Blade: Flow Visualization

Visualization of multiple vortex structures from unique tip shapes such as the subwing tip (Ref. 25) improve the understanding of how the tip shape can be used to modify the resulting tip vortex structure. For comparison, the flow visualization images were taken at the same wake ages as were used for the baseline blade. The resulting images are shown in Figs. 15 through 21, covering a wake age range from 10° to 209°. As with the baseline blade flow visualization, the scale is the same in the all the images. Figure 14 is a schematic of the first flow

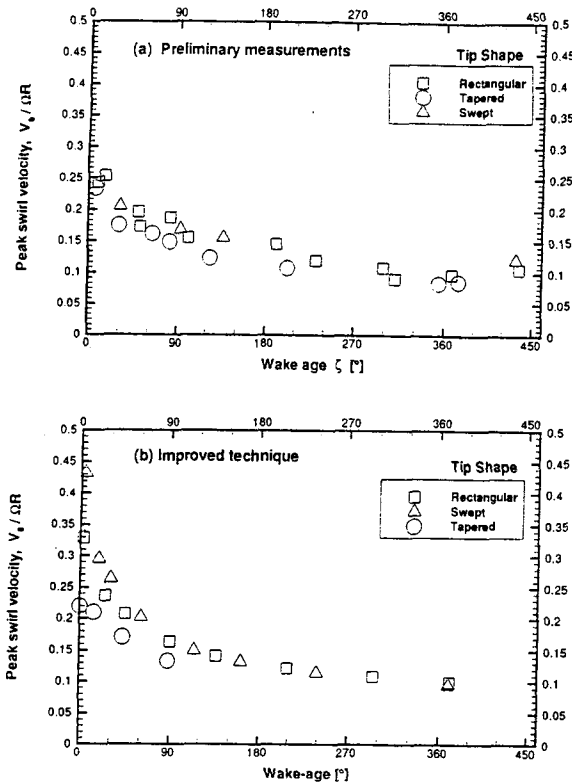


Figure 11: Variation of vortex peak swirl velocity (uncorrected) with wake-age (a) Preliminary measurements (b) Measurements using improved technique.

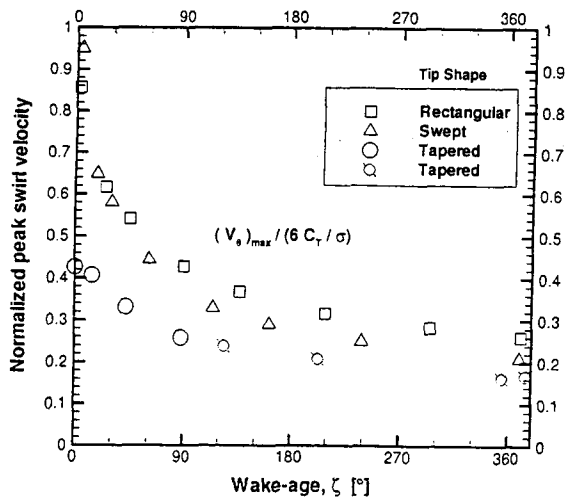


Figure 12: Variation of vortex peak swirl velocity normalized by blade loading with wake-age.

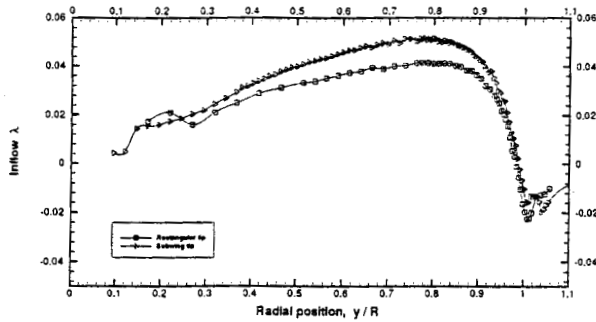


Figure 13: Phase-averaged inflow velocity measured in tip-path-plane of the subwing blade compared to the baseline.

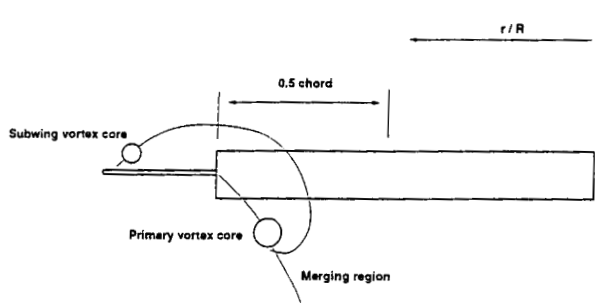


Figure 14: Schematic of the flow visualization image area for the subwing blade (only the outer 12% of main blade radius is shown, and the direction of rotation is out of the page).

visualization image at $\zeta = 10^\circ$, and gives an idea of the scale of the images. It can be seen in Fig. 14 that the subwing extends almost 4% radius outboard of the nominal blade radius, and the visible part of the blade corresponds to the outer 12% of the blade tip.

The first picture (Fig. 15) shows the subwing vortex immediately after formation, as the blade is rotating out of the plane of the page. The subwing vortex appears to originate at about the 80% radial station on the subwing. This was confirmed by slowly varying the phase of the image during the experiment. At this early wake age, the primary vortex from the main blade is not visible because optical access is blocked by the blade tip.

Figure 16 shows the trailed vortices at $\zeta = 25^\circ$, where the extreme tip of the blade can be seen on the far right. The vortex pair has rotated clockwise, with the subwing vortex moving axially up and radially inboard, and the primary vortex moving axially downward and slightly radially inboard. There is a clear difference in the appearance of the vortices, with the subwing vortex showing a well-defined seed void, while the primary vortex shows a less clearly defined region at its center. This in-



Figure 15: Flow visualization of wake generated by the subwing tip blade at $\zeta = 10^\circ$.

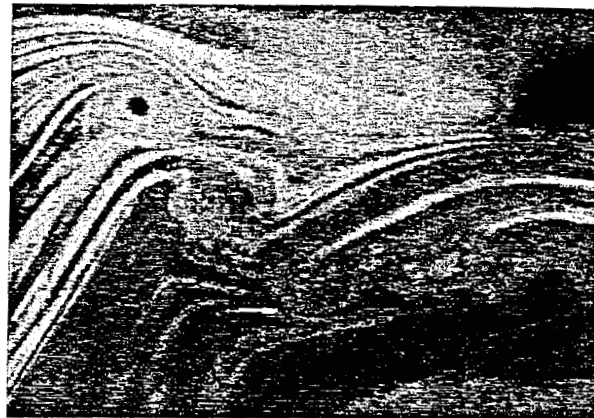


Figure 16: Flow visualization of the subwing tip blade at $\zeta = 25^\circ$.

dicates a relatively more diffuse primary vortex from the main blade compared to that produced by the subwing.

The vortices at a wake age of 45° are shown in Fig. 17. At this point, the pair has rotated in the light sheet plane about 100° from the original position, and the subwing vortex is now above the primary vortex. The vortex sheet can be seen to wrap up around the outboard side of the primary vortex.

The image in Fig. 18 shows the vortices at $\zeta = 67^\circ$. Here the vortex pair has rotated about 125° in the light sheet plane, and the primary vortex is now outboard of the subwing vortex. The subwing vortex lies in the tip-path-plane. At this point the two vortices can be seen to be beginning their merging process, as their structures seem to be undergoing some kind of interaction. The aperiodicity of the locations of the vortex cores was noted to increase at this point.



Figure 17: Flow visualization of the subwing tip blade at $\zeta = 45^\circ$.



Figure 19: Flow visualization of the subwing tip blade at $\zeta = 90^\circ$.



Figure 18: Flow visualization of the subwing tip blade at $\zeta = 67^\circ$.



Figure 20: Flow visualization of the subwing tip blade at $\zeta = 137^\circ$.

Figure 19 shows the vortices at $\zeta = 90^\circ$, where they have rotated about 180° in the light sheet plane and have now switched positions relative to their initial orientation. The seed voids are present, but there is obviously some interaction occurring between the vortices. The primary vortex, in particular, appears very diffuse and almost no clear structure can be seen. The vortex sheet is seen to still be in the process of being entrained into the primary vortex. The turbulent flow from the vortex sheet seems to be creating significant instability within the primary vortex and in the surrounding area.

At a wake age of 137° , as shown in Fig. 20, the vortices appear to have completed merging and are now essentially one tip vortex. However, the aperiodicity of the vortex core location was noted to still be significant at this wake age. A seed void is visible but it seems very diffuse. In fact, the entire vortex appears to be more

diffuse, and is surrounded by flow that appears to contain turbulent eddies. The vortex sheet has convected downward faster than the vortex core, and only the out-board edge of the sheet can be observed. However, the sheet appears to still be wrapping into the merged vortex, causing more turbulent flow to be entrained into the flow surrounding the core.

Results for the last wake age of 209° are shown in Fig. 21. No clearly laminar flow region can be seen. The vortex sheet has wrapped all the way around into the merged vortex. Note that as mentioned previously, these images are all to the same scale. The very large size of the seed void and of the overall vortex structure at this wake age confirms the increase in core radius expected from the merged vortices generated by the subwing tip blade.



Figure 21: Flow visualization of the subwing tip blade at $\zeta = 209^\circ$.

Subwing Blade: Measurement Technique

The creation of multiple vortices required a different technique to capture the vortex velocity profiles. Using the flow visualization results for the subwing blade, it was possible to construct radial measurement grids for the phase-resolved LDV measurements. These grids are shown in Fig. 22, along with a scale representation of the subsequently estimated vortex core sizes as detailed in Ref. 26. As with the baseline blade, the measurement grids were designed to extend between 5 and 10 core radii on either side of the vortices. Because of the extremely small physical size of the subwing vortices, the grids were constructed with center portions having spacing of 0.25 mm (0.5% c) between measurement points so as to accurately resolve the large velocity gradients surrounding the vortex core (the variable grid spacing is not shown in Fig. 22).

At the earliest wake ages, the difficulty of finding the exact location of the very small subwing vortex necessitated using a vertical measurement grid (parallel to the rotor shaft), rather than the standard radial grid. This ensured that the grid would capture the subwing vortex regardless of where it crossed vertically. Note that because two of the measured cases used vertical grids, their results cannot be plotted on the same axes as the other wake ages, and thus they are shown separately. However, to enable comparison, the plots are all shown with the same scale and orientation. This allows the results for the tangential and axial velocity components to be directly compared.

Subwing Blade: Vortex Trajectories

A closer view of the wake geometry in terms of the axial or vertical (z) and radial (y) locations of the vortices at

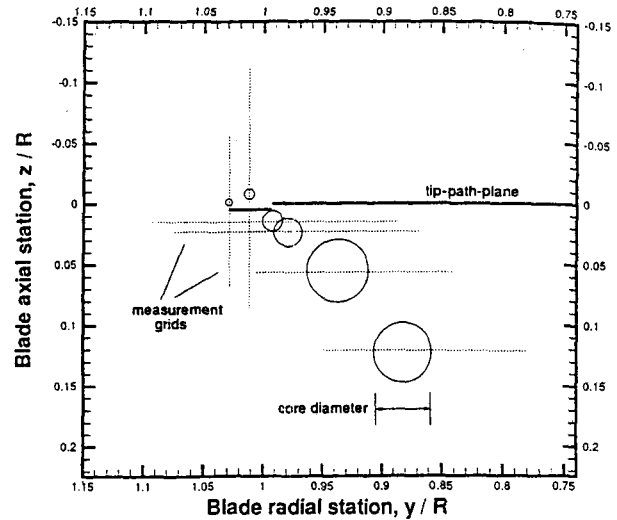


Figure 22: LDV measurement grids for the subwing blade.

each wake age measured is shown in Fig. 23. The wake ages measured with the subwing tip were from $\zeta = 8^\circ$ to $\zeta = 260^\circ$. It was found through experimentation that between about $\zeta = 40^\circ$ and $\zeta = 130^\circ$ the interaction and merging of the subwing and primary vortices created a less coherent vortical structure that could not be accurately measured because of excessive aperiodicity in the flow. While the flow at these wake ages could still be qualitatively analyzed through flow visualization, the statistically-based measurement nature of LDV made it extremely difficult to obtain meaningful results in this region. After the merging region, the vortex could again be measured with aperiodicity levels of the same order as the baseline. Detailed aperiodicity measurements were not made, however, as in the case of the baseline blade.

It can be seen that the subwing vortices at the two earliest wake ages ($\zeta = 8^\circ$ and 22°) lie outboard of the blade tip (where $y/R = 1$ is the tip of the main blade), and at the second wake age ($\zeta = 22^\circ$) the vortex additionally lies above the tip path plane (i.e., $z/R < 0$). This is a result of the rotation of the subwing vortex around the stronger main tip vortex.

Subwing Blade: Tangential Velocity Profiles

The vortex-induced tangential velocity profiles, normalized by the rotor tip speed, are shown in Figs. 24 and 25. The subwing vortex and the primary vortex were studied independently, because only one vortex was targeted per LDV traverse across the flow field. One of the most significant contributions of this work is simply

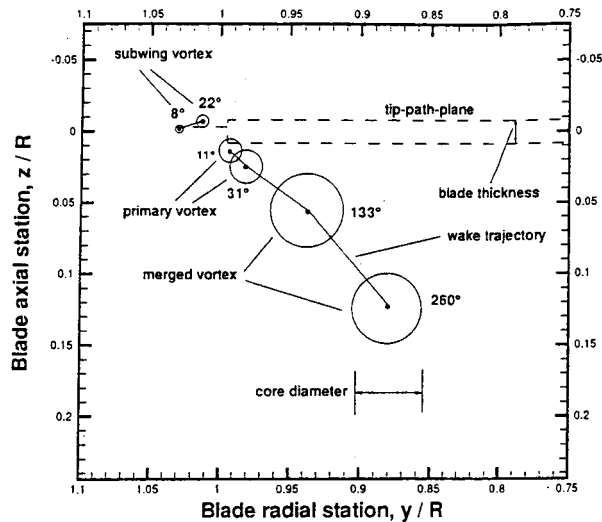


Figure 23: Subwing blade vortex locations relative to tip-path-plane.

the process of capturing these highly dynamic interacting vortices before and after the merging process. It is important to note that before the merging process there are two vortices present in the flow, so neither vortex can be isolated from the induced effects of the other in these types of experiments. For this reason, asymmetries in the profiles are very different than in the case of the baseline blades. It is not very accurate to deduce from the measurements any vortex properties (e.g., core radius and peak swirl velocity) that inherently assume a single isolated vortex. In fact, it is the interaction of the induced velocity fields that drives the merging process. Keeping this limitation in mind, results are shown in an effort to provide best estimates of these properties. The measurement grids shown in Fig. 22 were chosen, in part, to minimize the signature of the adjacent vortex. The purpose is to understand the dynamics and timing involved in the merging process. The most accurate results (and the most practical) are the final vortex properties and structure after the merging process. The reason is that the final merged vortex structure is what (in most cases) would be encountered by a following blade.

Subwing Blade: Axial Velocity Profiles

The axial velocity profiles, normalized by the tip speed, for each of the six measured wake ages are shown in Figs. 26 and 27. Again the subwing and primary vortices were measured with different grid orientations, and so are shown separately.

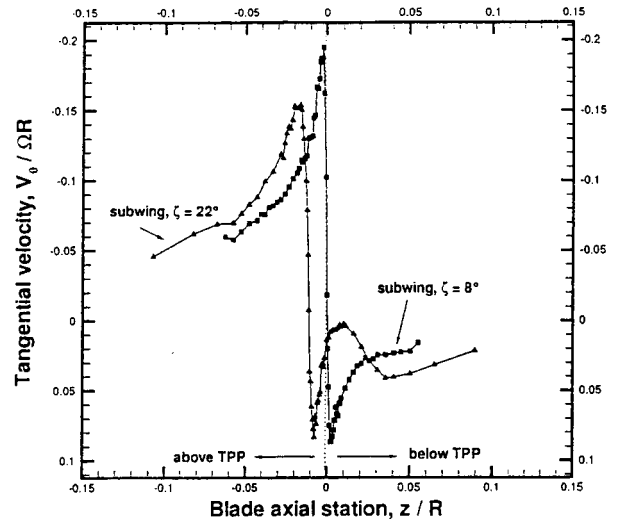


Figure 24: Measured tangential velocity profiles of subwing vortices at two wake ages.

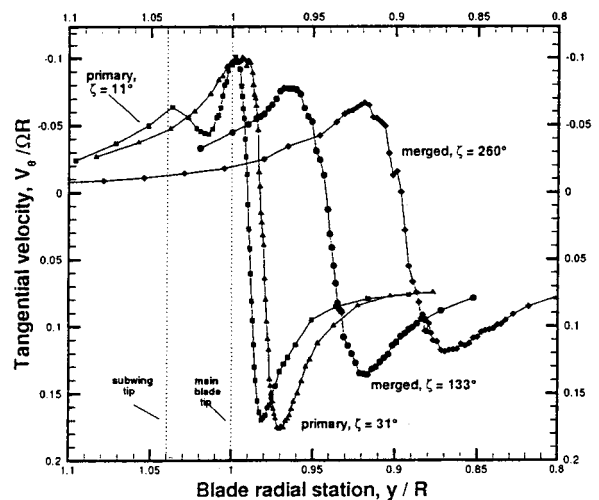


Figure 25: Measured tangential velocity profiles of primary and merged vortices at four wake ages.

It can be seen from Fig. 27 that at the early wake ages, the primary vortex has axial velocities of comparable magnitude to the tangential velocities. From the stability analysis of Ref. 26, the stability of the vortex core is a function of the ratio of peak swirl velocity to peak axial velocity deficit. In this case, both cores would be considered unstable according to the peak values shown in

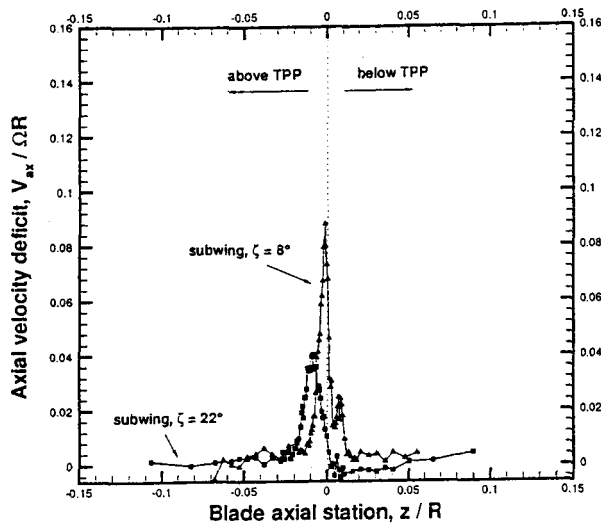


Figure 26: Measured axial velocity profiles of subwing vortices at two wake ages.

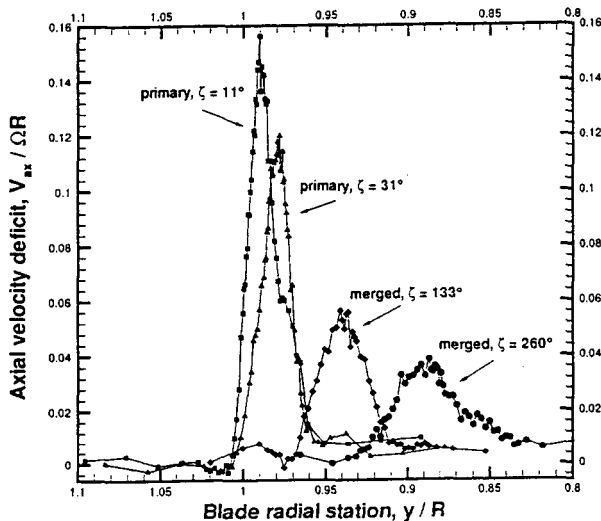


Figure 27: Measured axial velocity profiles of primary and merged vortices at four wake ages.

Figs. 25, 24, 26, and 27. This appears to be consistent with the bands of turbulent flow surrounding both cores observed in the flow visualization results. The axial velocity peak rapidly decreases after the merging process is complete. The width of the axial velocity deficit region appears to be 2 to 3 times the core radius on each

side of the vortex, as in the case of the baseline blade. In terms of axial and tangential velocity profiles, the final structure of the core appears to be very similar to the baseline blade once the merging process is complete.

Subwing Blade: Vortex Properties

The vortex core properties can be estimated from the velocity measurements, keeping in mind the above mentioned limitations concerning the difference between an isolated vortex and a pair of vortices. One of the primary effects of the subwing blade is a significant increase in the net core size after the merging process. Figure 28 shows the change in estimated viscous core radius with wake age, normalized by the blade chord. As with the baseline blade, the vortex core radius is defined to be half the distance between the measured peaks in the tangential velocity.

At the earliest wake age of $\zeta \approx 10^\circ$, the core radius of the subwing vortex was estimated to be 2.5% of the blade chord, while the core of the primary vortex was 7.7% chord. The core grows to about 23% chord after the vortices have merged, and stays nominally constant thereafter. By comparing the subwing blade with the baseline, the core radius appears to be approximately double just after the merging process is complete. A large increase in core radius would be an advantage for alleviation of noise and vibratory airloads, especially if the peak swirl velocity decreased by the same factor.

These measurements show this might not be the case, however, because the merging process appears to redistribute the vortex circulation distribution. In the flow visualization and the measurements, both the subwing and primary vortex appear to rapidly diffuse before the merging. Accurate modelling of this type of blade tip requires the ability to capture both the individual diffusion of each vortex core, and the global merging process. The entire process appears to be the result of a viscous-inviscid interaction. Even these basic measurements pose a tough challenge for current modeling capabilities.

This redistribution of circulation is shown by the variation of non-dimensional peak tangential velocity, $V_{\theta_{max}}/\Omega R$, with wake age, ζ , shown in Fig. 29. For comparison, the baseline measurements (uncorrected) are also shown in this figure. The primary difference between the baseline and the subwing blades is that the subwing blade has a very small change in peak swirl velocity with wake age. The reason for this is an inviscid-viscous interaction that results in almost no net change in the swirl velocity as the vortex ages.

The interaction is described as follows. The total vortex strength trailed behind the blade is divided between the two vortices. When the vortices merge, the effective

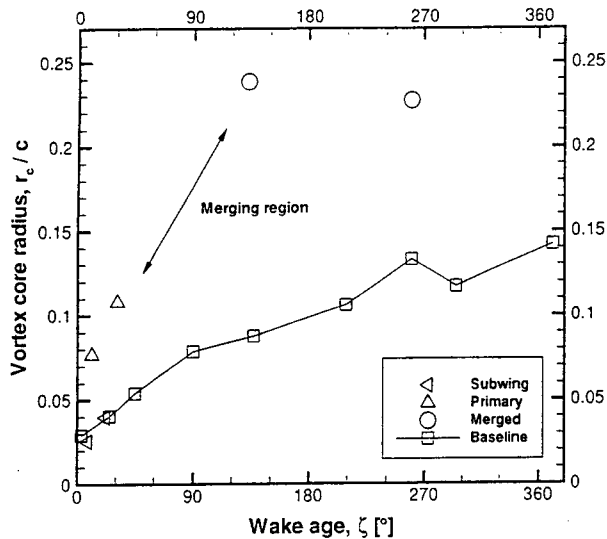


Figure 28: Vortex core radius versus wake age for the subwing blade compared to the baseline.

circulation approximately doubles from the value each core showed before merging. This is the inviscid part of the interaction – which can be predicted by potential flow vortex conservation laws. The viscous part of the interaction is that the effective core size increases by roughly a factor of two from that of the largest core before merging. It was shown in Ref. 26 that the peak swirl velocity is by definition proportional to the ratio of the vortex circulation to core radius. A doubling of the circulation and a doubling of the effective core radius cancel. This results in a very small change in the peak swirl velocity after merging. In these tests the circulation is not equally divided, and so there is a reduction in the peak swirl velocity when the comparison is made by normalizing with blade loading (as shown by Fig. 30). The benefit in terms of reduced peak swirl velocity appears to decrease with wake age, however, more measurements are required.

These results are supported by the flow visualization images at $\zeta = 209^\circ$. The vortex from the baseline blade [Fig. 31(a)] has a clear seed void at its center, surrounded by a small region of relatively smooth stratified flow. Further out, the flow becomes much more turbulent, with eddies being visible. The merged vortex from the subwing tip blade has a seed void, but it is much less clearly defined [Fig. 31(b)]. Also, nowhere does the flow appear to be smooth and laminar. Turbulent flow is seen to completely surround the vortex core.

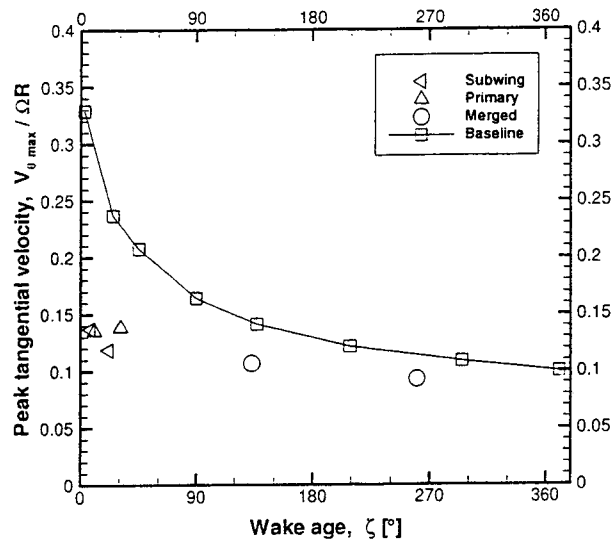


Figure 29: Vortex peak tangential velocity versus wake age for the subwing blade compared to the baseline.

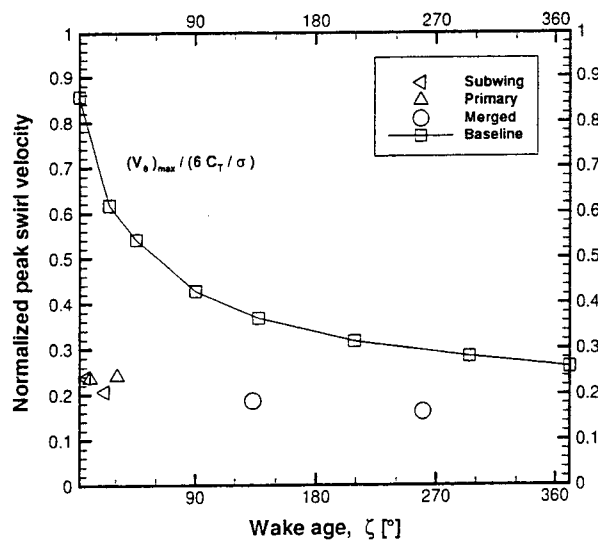
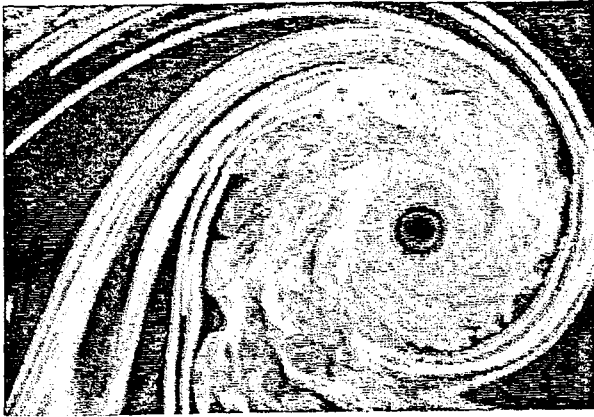


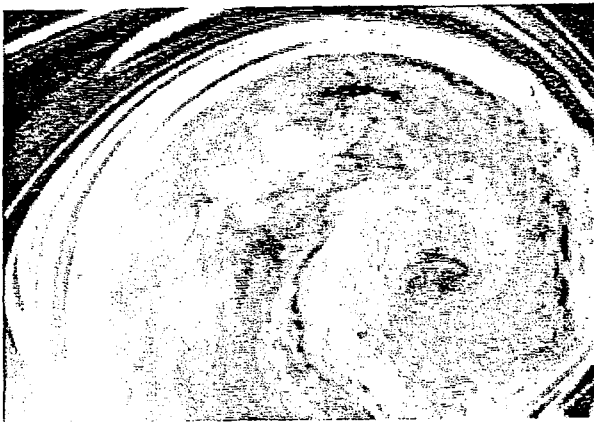
Figure 30: Vortex peak tangential velocity normalized by blade loading versus wake age for the subwing blade compared to the baseline.

Subwing Blade: Scale Effects

From the subwing results, the merging process is assumed to be a strong function of the vortex Reynolds number. For this reason, the same type of increase in core radius might not be observed at full-scale flight



(a) Baseline blade wake



(b) Subwing tip blade wake

Figure 31: Comparison of flow visualization of wake at $\zeta = 209^\circ$.

Reynolds numbers. More research is needed to understand the vortex structure that would be formed in forward flight. These tests, however, show that it is an advantage to divide the circulation between two vortices in terms of the magnitude of the initial peak swirl velocity. It appears the benefit is reduced as the vortices merge in comparison with the baseline blade. It is concluded in terms of BVI noise reduction, that designs aimed at dividing the circulation while preventing merging might be an advantage over the subwing blade – especially at late wake ages where the most severe parallel interactions occur.

Analysis of Baseline Vortex Measurements

The baseline blade measurements were first reported in Ref. 23. Recently, more detailed analysis of the data has

provided insight into the basic fluid mechanics. These results are presented here in terms of vortex structure and vortex core stability. An understanding of both of these topics supports the development and analysis of tip vortex alleviation devices.

Iverson's Equation

Iverson (Ref. 34) developed a correlation function based on the self-similar turbulent decay of a line vortex. The objective of developing a correlation function was to understand the scale effects involved in measuring vortices in low Reynolds number facilities compared to the actual high Reynolds number behavior measured in flight tests. The purpose of solving Iverson's equation is to determine a similarity solution for the vortex velocity profiles for the case when a turbulent viscosity is allowed to vary across the vortex. The importance of obtaining a similarity solution is that it is an exact solution of the Navier-Stokes equations, which is useful for developing fundamental vortex models such as the Lamb vortex. A unique aspect of Iverson's result is the Reynolds number dependence on the final solution, which does not occur in the case of the Lamb vortex.

The vorticity transport equation with a variable eddy viscosity was given by Iverson in terms of circulation

$$\frac{\partial \Gamma}{\partial t} = r \frac{\partial}{\partial r} \left(v_T r \frac{\partial}{\partial r} \left(\frac{\Gamma}{r^2} \right) \right) + 2v_T r \frac{\partial}{\partial r} \left(\frac{\Gamma}{r^2} \right) \quad (6)$$

where the turbulent viscosity is a function of the distance from the center of the core and the local circulation strength

$$v_T = \frac{\alpha^2 r^2}{2\pi} \left| r \frac{\partial}{\partial r} \left(\frac{\Gamma}{r^2} \right) \right| + v \quad (7)$$

This is equivalent to specifying a variable mixing length as

$$l = \alpha r \quad (8)$$

where the empirical constant according to Iverson is

$$\alpha = 0.01854 \quad (9)$$

This equation is non-dimensionalized in order to obtain a single equation that provides a similarity solution

$$\frac{\partial^2 \gamma}{\partial \eta^2} \left(4 \left| \eta \frac{\partial \gamma}{\partial \eta} - \gamma \right| + \frac{2\pi}{\alpha^2} \frac{1}{Re_v} \right) = - \frac{\partial \gamma}{\partial \eta} \quad (10)$$

with the similarity variables

$$\eta = \frac{r^2}{4\alpha^2 \Gamma_v \tau}, \quad \tau = t + t_0, \quad \gamma = \frac{\Gamma}{\Gamma_v}, \quad Re_v = \frac{\Gamma_v}{v} \quad (11)$$

This equation will be referred to as Iverson's equation. The solution (outlined in Ref. 26) provides a self-similar

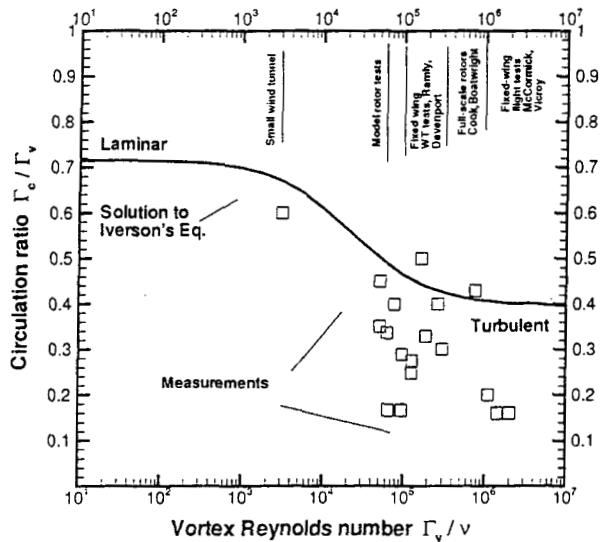


Figure 32: Vortex core strength as a function of Reynolds number obtained by solving Iverson's equation compared to several sets of measurements compiled in Ref. 26.

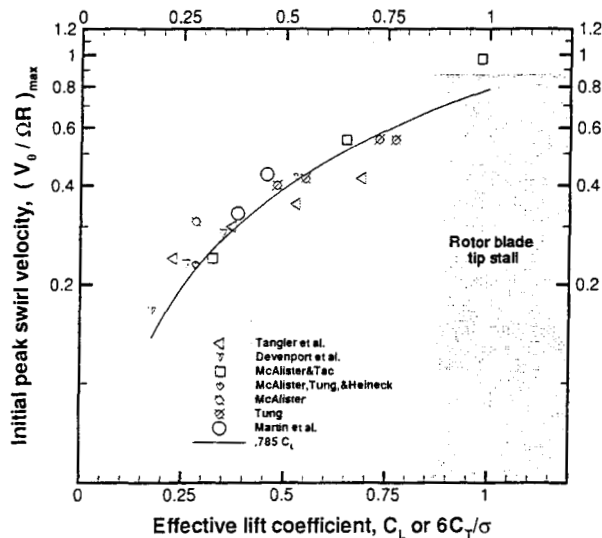


Figure 33: Vortex initial peak swirl velocity as a function of effective lift coefficient for rotor-blades and non-rotating wings (from Ref. 26).

circulation profile, $\gamma(\eta)$ across the vortex core. This type of profile helps to describe the structure of the vortex.

The core strength $\gamma(1) = \Gamma_c/\Gamma_v$ is found to be a function of vortex Reynolds number, as shown in Fig. 32. At low Reynolds numbers the fully laminar solution is

identical to the Lamb vortex. At high Reynolds numbers the fully turbulent solution is another fundamental exact solution for a vortex flow. As shown by the results in Fig. 32, most experiments have been made in the transitional range of the solution. The advantage of Iverson's method is that it provides some fundamental self-similar profiles to use for comparing experimental data. The disadvantage is that the prediction of the core strength does not appear to agree with available measurements. This is shown by the comparison between the theory and measurements in Fig. 32 of the ratio Γ_c/Γ_v . One possible reason for this is that 2-D vortex models based on a solution of the Navier-Stokes equation do not take into account the variation of the initial core structure with lift coefficient (i.e., the initial conditions at t_0 vary with the blade lift). This is discussed by McCormick (Ref. 35), and is supported by the variation of initial peak swirl velocity with lift coefficient shown in Fig. 33.

Furthermore, other factors may influence the role of turbulence in the core structure, such as tip separation effects, boundary layer states near the trailing edge, and roll-up of the trailing vortex sheet. For this reason, aircraft vortices might not be properly modeled by the ideal laminar or ideal turbulent solutions for an isolated two-dimensional vortex.

Extension of Iverson's Result to Transitional Vortices

The baseline measurements in this study appear partly laminar and partly turbulent (see Ref. 26), and so these two fundamental solutions are superimposed to obtain a model for transitional vortices. The important question is where the vortex transitions from laminar to turbulent, and the ability to predict this behavior. A preliminary answer to this question can be found using the concept of relaminarization and the Richardson number formulation presented in Ref. 26.

Using the definition of a shape factor applied to Iverson's equation

$$S_p = \frac{V_\theta/r}{dV_\theta/dr} \approx \frac{\gamma}{(\eta/\eta_c)} \frac{2\pi}{\gamma \ln(\sqrt{\eta/\eta_c}) + 2d\gamma/d\eta} \quad (12)$$

the Richardson number is

$$Ri = 2S_p(S_p + 1) \quad (13)$$

The procedure begins with obtaining three solutions for the vortex using Iverson's method. One solution is fully turbulent γ_T , one is fully laminar γ_L , and one is at the given vortex Reynolds number $\gamma(Re_v)$.

The next step is to test for relaminarization, where the test parameter is defined as (Ref. 26)

$$R_L = \frac{R_i}{Re_v^{1/4}} \quad (14)$$

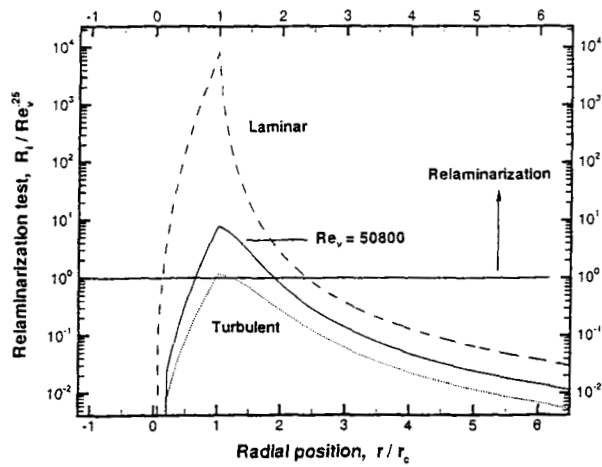


Figure 34: Distribution of Richardson number across vortex in terms of R_L .

When $R_L < 1$ no relaminarization can occur, and when $R_L > 1$ the streamline curvature limits the role of turbulence in transporting vorticity.

Figures 34 and 35 show the distribution of R_L outside of the core for the three cases. In the case of the fully turbulent vortex, R_L remains less than one, and in the case of the fully laminar vortex, R_L remains greater than one over the region where 99% of the vorticity is contained. For the case of $Re_v = 50800$ (which corresponds to the baseline test case), the value of R_L becomes less than 1 near $r/r_c = 2$. Using the value of R_{Lc} at the core boundary, a transitional circulation profile γ_{tr} is constructed by superposition of the fully laminar γ_L and fully turbulent γ_T profiles. The superposition is accomplished using a form of the Gudermannian function

$$f = \frac{2}{\pi} \tan^{-1} \left(\exp \left(\frac{r}{r_c} - \frac{1}{2} R_{Lc} \right) \right) \quad (15)$$

The transitional circulation profile is then

$$\gamma_{tr} = f \gamma_T + (1 - f) \gamma_L \quad (16)$$

and the corresponding velocity profile is shown in comparison with the measurements in Fig. 36. The result is in agreement with the measurements.

Repeating this procedure over a range of Reynolds numbers creates a family of transitional vortex profiles. The only unknown is the radial position where 50% of the transition takes place, $\frac{1}{2} R_{Lc}$. The variation of R_{Lc} with Reynolds number is shown in Fig. 37. This figure shows the range of Reynolds numbers where the vortex might appear transitional. More research is needed in this area.

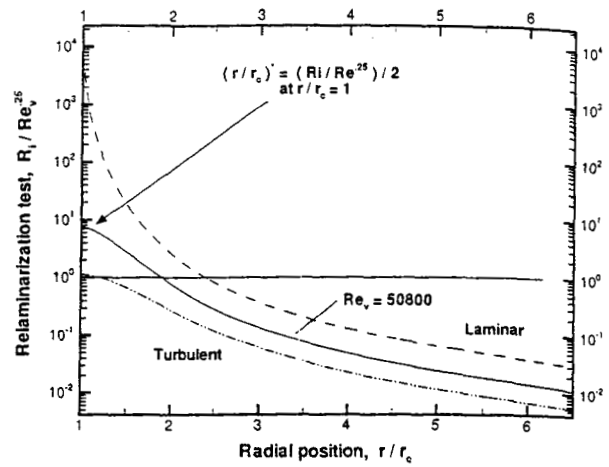


Figure 35: Transition point defined by relaminarization test.

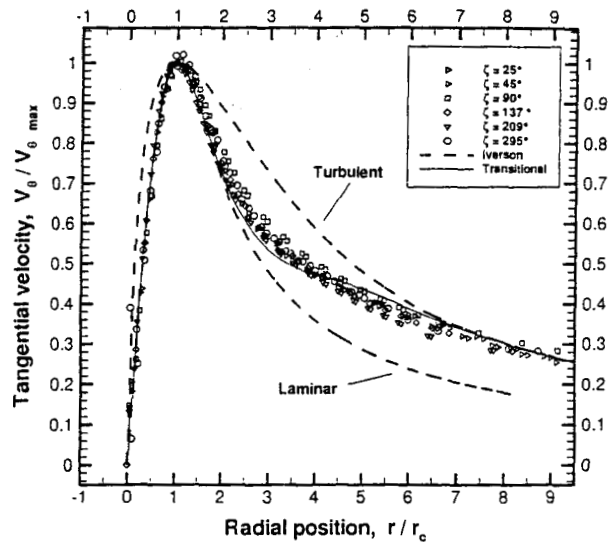


Figure 36: Transitional vortex velocity profile $Re_v = 50800$ compared to laminar and turbulent profiles and measurements, $Re_v = 50800$.

Vortex Core Stability

Another decay mechanism that may also participate in the core growth of rotor vortices is the stability of the vortex core. This is related to axial flow and can be described by an adaptation of the Leibovich-Stewartson vortex stability theory (Ref. 36, 37). This practical theory is applied by first fitting the following Lamb-like

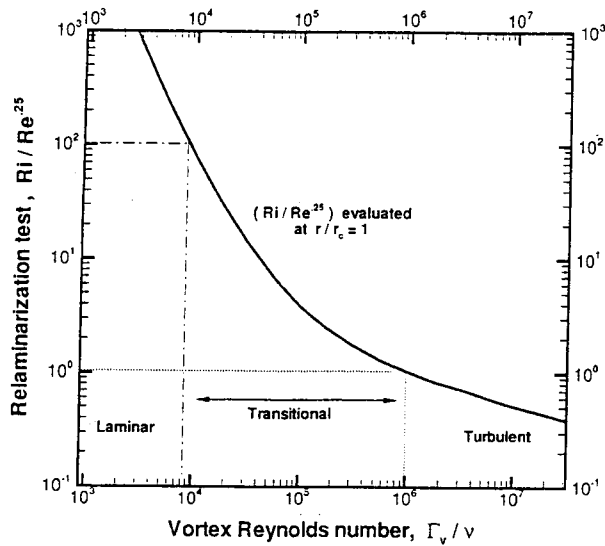


Figure 37: The variation of R_{L_c} with Reynolds number obtained from the solution of Iverson's equation.

functions to the measured velocity distributions using

$$\frac{V_\theta}{\Omega R} = \frac{A}{r} (1 - e^{-Br^2}) \quad (17)$$

$$\frac{V_{ax}}{\Omega R} = C e^{-Dr^2} \quad (18)$$

where the unknown coefficients are $A, B, C,$ and D . The stability parameter is then defined by

$$S = \frac{V_{\theta max}}{\Omega R} \left(\frac{D}{BC} \right) \quad (19)$$

and the vortex core is considered unstable when $S < 0.9$ (Ref. 38). Using this criteria, the present measurements of peak axial and swirl velocity show that $S = 0.65$, so that initially the vortex at $\zeta = 3^\circ$ may be unstable, and by a significant margin. This is a sufficient condition for the vortex to undergo a "hydraulic jump" to a larger diameter, or even burst (Ref. 38). The "hydraulic jump" process is described by Rule (Ref. 39), and is supported by the measurements of the changing core circulation structure in Ref. 26. The strength of this instability is proportional to the ratio of the peak swirl velocity to the axial velocity deficit.

The Leibovich-Stewartson vortex stability theory considers only the general structure of the entire core. The final conclusion is that the core is either stable or unstable, but there is no indication of how the different regions of the vortex core contribute to the stability. Detailed modeling of the vortex, as well as effective alleviation strategies, requires an understanding of which regions of the vortex are the most stable and unstable. This

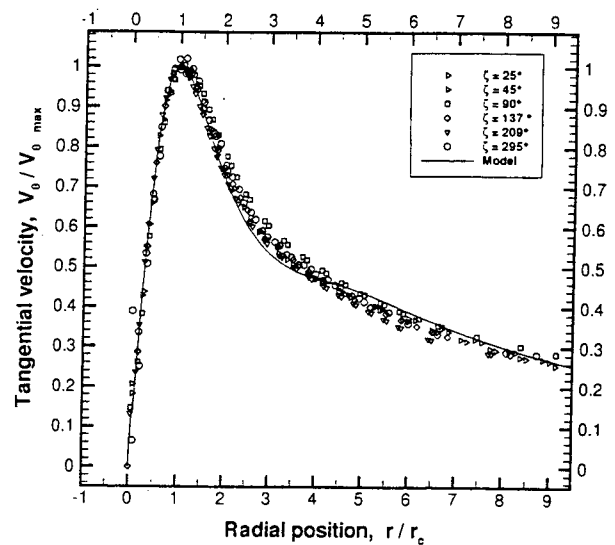


Figure 38: Self-similar tangential velocity distribution compared to transitional Iverson model.

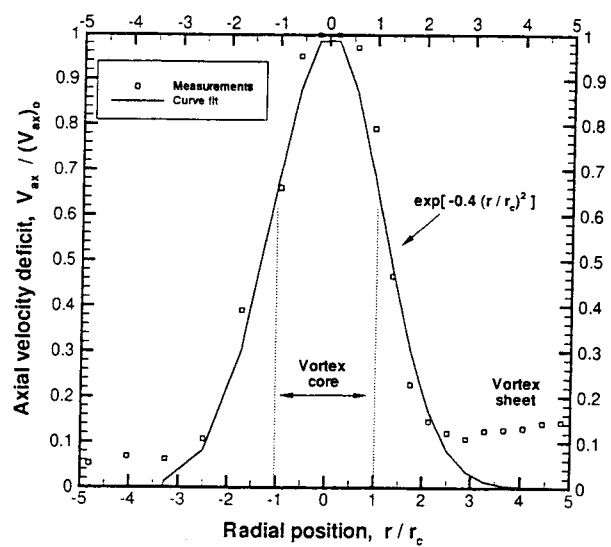


Figure 39: Self-similar axial velocity distribution estimated from early wake age measurement at $\zeta = 3^\circ$.

is very similar to the analysis of boundary layers, where the mean flow properties are used to determine a shape factor, H , that allows the regions of laminar and turbulent flow to be estimated. For vortex flows the same type of procedure involves using the Ludwig stability test (Ref. 40) to classify regions of the core as either stable or unstable in terms of the ability to produce or damp out turbulence.

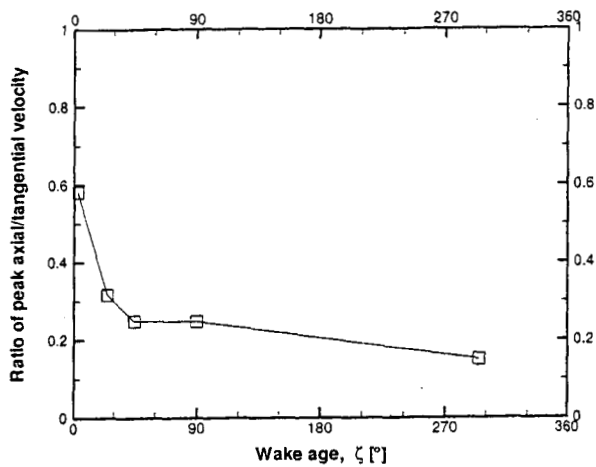


Figure 40: Ratio of peak axial velocity to peak swirl velocity as a function of wake age.

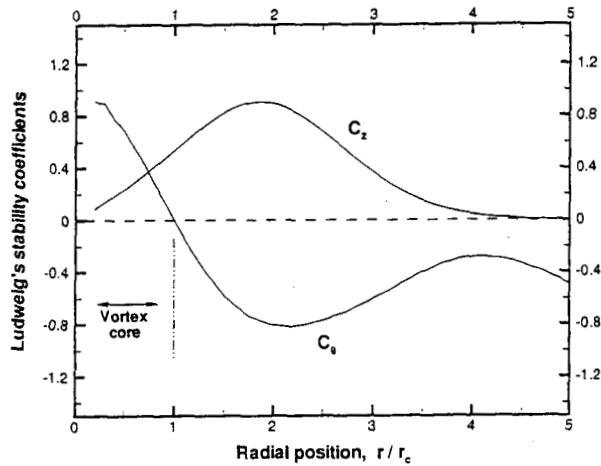


Figure 41: Ludwig's stability coefficients as a function of the radial position across the vortex.

The procedure for calculating the Ludwig stability map of the vortex core requires both the tangential and axial velocity profiles. These have been measured in the current experiments and can be used along with the theory to estimate the vortex structure from the mean flow properties. The Ludwig stability theory involves two coefficients that are simply a measure of the ratio of the local velocity gradient to the local angular velocity of the fluid. One coefficient is determined from the tangential velocity distribution

$$C_\theta = \frac{d\bar{V}_\theta}{d\bar{r}} \left(\frac{\bar{r}}{\bar{V}_\theta} \right) \quad (20)$$

where all of the variables are assumed to be self-similar

values determined from the measured profile shown in Fig. 38. The other coefficient is determined from the axial velocity deficit measured at the earliest wake age – see Fig. 39

$$C_z = -\frac{(V_{ax})_0}{(V_\theta)_{max}} \left(\frac{d\bar{V}_{ax}/d\bar{r}}{\bar{V}_\theta/\bar{r}} \right) \quad (21)$$

Note the sign convention of V_{ax} is that a deficit (wake-like profile) is a positive increment from the free-stream velocity. The maximum value at the center of the profile is $(V_{ax})_0$. The coefficient C_z is also a function of the ratio of the peak axial velocity to the peak swirl velocity.

The variation of the tangential and axial coefficients is shown in Fig. 41. In this figure, it was assumed that the ratio of the peak axial velocity to the peak swirl velocity was one, so that the results can be scaled for different wake ages by multiplying C_z by the actual ratio shown in Fig. 40. In addition, a curve fit to both profiles was used to calculate the velocity gradients. The curve fit to the axial profile is shown as a simple exponential distribution in Fig. 39. The curve fit to the tangential velocity profile shown in Fig. 38 is the transitional Iverson result as derived.

The final step after the coefficients have been determined is to make a comparison with the stability boundary. The stability boundary is a function of these two coefficients, and Ludwig's condition for stability is defined (Ref. 40) by the inequality

$$(1 - C_\theta)(1 - C_\theta^2) - C_z^2 \left(\frac{5}{3} - C_\theta \right) > 0 \quad (22)$$

By plotting the values of C_θ versus C_z for different radial positions from the vortex center, the stability of different regions of the vortex core can be estimated with respect to the stability boundary shown in Fig. 42. As shown in this figure, there is a band of radial positions where the vortex structure is estimated to be unstable, and therefore capable of producing turbulence. This appears to correlate well with the flow visualization image shown in Fig. 44. As the ratio of the peak axial velocity to peak swirl velocity decreases with wake age (Fig. 40), the measured curve would scale below the stability boundary and the vortex would become stable.

A more physical presentation of the same result can be obtained by plotting the difference between the measured results and the stability boundary, as shown in Fig. 43. The fundamental result obtained by applying the Ludwig stability test to measurements at the earliest wake age of 3° is that the vortex core is stabilized by the rotational flow. These results show that if there is a turbulence producing region of the vortex, it would appear outside the core boundary from $r/r_c = 1.5$ to $r/r_c = 2.75$. This result is important because most

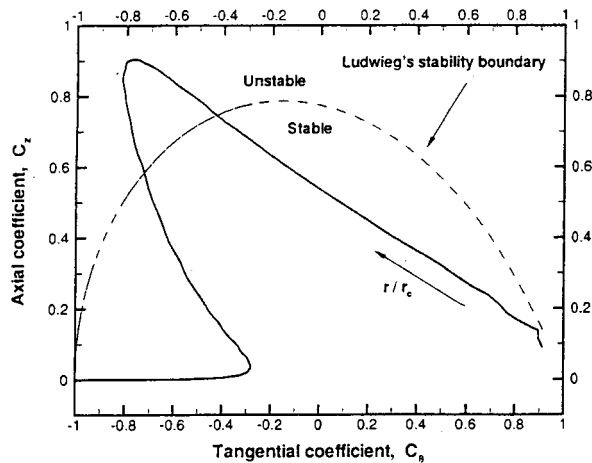


Figure 42: Ludweig's stability map.



Figure 44: Flow visualization image zoomed-in on the vortex core region.

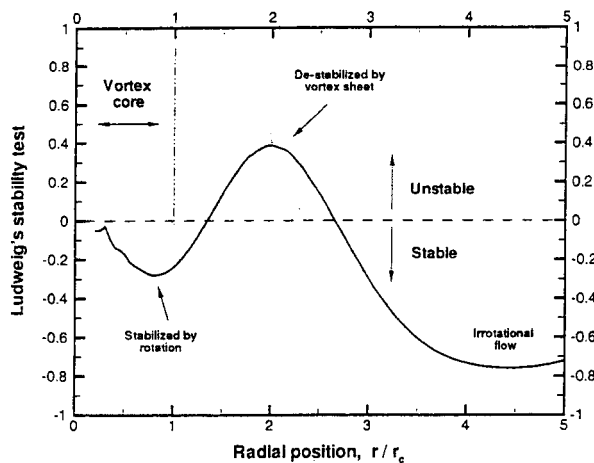


Figure 43: Ludweig's stability test as a function of position across the vortex core.

vortex alleviation devices attempt to promote turbulence inside the vortex core where instabilities are quickly damped by the high streamline curvature. By using detailed measurements and stability analysis, future vortex alleviation devices might be designed to take advantage of the unstable region outside of the core. In theory, such a device would not have the severe drag penalty of typical devices designed to increase the axial velocity deficit inside the core. More research is needed to confirm this hypothesis.

Conclusions

Three-dimensional phase-resolved laser Doppler velocimetry measurements with high spatial and temporal resolution were made in the viscous wake trailing from a helicopter rotor blade. Detailed velocity profiles of the trailing vortex filament enabled the study of the vortex core formation, vortex roll-up, and vortex evolution. The conclusions drawn from this study are as follows:

1. One of the primary differences shown by the change in tip shape was the measured wake geometry. Tip sweep appeared to decrease both the radial and axial convection of the core, while taper appeared to increase the radial convection and decrease the axial convection. These results are for hover, and more research is needed to conclude the same effects would apply to forward flight.
2. While there was little difference in the measured vortex core growth between the various tip shapes, differences were observed in the peak swirl velocity. After the blade loading variation between tests is used to normalize the peak swirl velocity, the swept and baseline blades showed similar behavior. The effect of blade taper was to reduce the initial peak swirl velocity by a significant fraction. It appears that this is accomplished by decreasing the peak bound circulation (and therefore the trailed vortex strength) for a given blade loading.
3. The subwing measurements showed that between the wake ages of $\zeta = 40^\circ$ and $\zeta = 130^\circ$, the in-

teraction and merging of the subwing and primary vortices created a less coherent vortical structure. In terms of axial and tangential velocity profiles, the final structure of the core generated by the subwing blade appears to be very similar to the baseline blade after the merging process is complete. The primary difference between the baseline and the subwing blades is that the subwing blade has a very small change in peak swirl velocity with wake age and a much larger core size.

4. One source of vortex core instability is the ratio of the peak swirl velocity to the axial velocity deficit. These results show that if there is a turbulence producing region of the vortex structure, it is predicted to be outside of the core boundary from $r/r_c = 1.5$ to $r/r_c = 2.75$. This is the region where the measured vortex self-similar velocity profiles appear to transition from a laminar to a more turbulent model.

Acknowledgments

This work was supported by the National Rotorcraft Technology Center under Grant NCC 2944. Dr. Thomas Doligalski and Dr. Yung Yu were the technical monitors. The measurements of the subwing blade were made by Greg Pugliese, and the authors greatly appreciate the assistance of Mr. Pugliese with these and other test cases.

References

- ¹Rossow, V. J., "Lift-generated Vortex Wakes of Subsonic Transport Aircraft" *Progress in Aerospace Sciences*, Vol. 35, 1999, pp. 507-660.
- ²Spalart, P. R., "Airplane Trailing Vortices," *Annual Review of Fluid Mechanics*, Vol. 30, 1998, pp. 107-138.
- ³Simons, I. A., Pacifico, R. E., and Jones, J. P., "The Movement, Structure, and Breakdown of Trailing Vortices from a Rotor Blade," Presented at the CAL/USAA Avlabs Symposium, Buffalo, NY, June 1966.
- ⁴Cook, C. V., "The Structure of the Rotor Blade Tip Vortex," AGARD-CP-111, 1973.
- ⁵Boatwright, D. W., "Measurements of Velocity Components in the Wake of a Full-Scale Helicopter Rotor in Hover," USAAMRDL Technical Report 72-33, 1972.
- ⁶Tangler, J. L., Wohlfeld, R. M., and Miley, S. J., "An Experimental Investigation of Vortex Stability, Tip Shapes, Compressibility, and Noise for Hovering Model Rotors," NASA CR-2305, 1973.
- ⁷Caradonna, F. X. and Tung, C., "Experimental and Analytical Studies of a Model Helicopter Rotor in Hover," *Vertica*, Vol. 5, 1981, pp. 149-161.
- ⁸Tung, C., Pucci, Caradonna, F. X., and Morse, H. A., "The Structure of Trailing Vortices Generated by Model Rotor Blades," *Vertica*, Vol. 7, 1983, pp. 33-43.
- ⁹Landgrebe, A. J., and Johnson, B. V., "Measurements of a Model Helicopter Rotor Flow Field With a Laser Doppler Velocimeter," *Journal of the American Helicopter Society*, Vol. 19, No. 3, 1974, pp. 39-43.
- ¹⁰Lorber, P. F., Stauter, R. C., and Landgrebe, A. J., "A Comprehensive Hover Test of the Airloads and Airflow of an Extensively Instrumented Model Helicopter Rotor," 45th Annual Forum of the American Helicopter Society, Boston, MA, May, 1989, pp. 281-295.
- ¹¹Raffel, M., Seelhorst, U., and Willert, C., "Vortical Flow Structures at a Helicopter Rotor Model Measured by LDV and PIV," *Aeronautical Journal*, Vol. 102, No. 1014, 1998, pp. 221-227.
- ¹²McAlister, K. W., Schuler, C. A., Branum, L., and Wu, J. C., "3-D Wake Measurements Near a Hovering Rotor for Determining Profile and Induced Drag," NASA TP-3577, ATCOM TR 95-A-006, 1995.
- ¹³Boutier, A., Lefevre, J., and Micheli, F., "Analysis of Helicopter Blade Vortex Structure by Laser Velocimetry," *Experiments in Fluids*, Vol. 21, 1996, pp. 33-42.
- ¹⁴Thompson, T. L., Komerath, N. M., and Gray, R. B., "Visualization and Measurement of the Tip Vortex Core of a Rotor Blade in Hover," *Journal of Aircraft*, Vol. 25, No. 12, 1988, pp. 1113-1121.
- ¹⁵Leishman, J. G., Baker, A., and Coyne, A., "Measurements of Rotor Tip Vortices Using Three-Component Laser Doppler Velocimetry," *Journal of the American Helicopter Society*, Vol. 41, No. 4, 1996, pp. 342-353.
- ¹⁶Heineck, J. T., Yamauchi, G. K., Wadcock, A. J., and Lourenco, L., "Application of Three-Component PIV to a Hovering Rotor Wake," 56th Forum of the American Helicopter Society, Virginia Beach, VA, May, 2000.
- ¹⁷McAlister, K. W., Tung, C., and Heineck, J. T., "Devices That Alter the Tip Vortex of a Rotor," NASA TM-2001-209625, AFDD TR-01-A-003, Feb., 2001.
- ¹⁸Martin, P. B., Pugliese, G. J. and Leishman, J. G., "Stereoscopic PIV Measurements in the Wake of a Hovering Rotor," 56th Annual Forum of the American Helicopter Society, Virginia Beach, Virginia, 2000.

- ¹⁹Bhagwat, M. J. and Leishman, J. G., "Correlation of Helicopter Rotor Tip Vortex Measurements," *AIAA Journal*, Vol. 38, No. 2, pp. 301-308, 2000.
- ²⁰Bhagwat, M. J. and Leishman, J. G., "Measurements of Bound and Wake Circulation on a Helicopter Rotor," *Journal of Aircraft*, Vol. 37, No. 2, March-April, 2000.
- ²¹Bhagwat, M. J. and Leishman, J. G., "On the Relationship Between Blade Lift and the Tip Vortex Characteristics," American Helicopter Society 54th Annual Forum, May 1998.
- ²²Martin, P. B., Bhagwat, M. J. and Leishman, J. G., "Strobed Laser-Sheet Visualization of a Helicopter Rotor Wake," *Journal of Flow Visualization and Image Processing*, Vol. 9, No. 1, 2000, pp. 31-50.
- ²³Martin, P. B., Pugliese, G. J., and Leishman, J. G., "High Resolution Trailing Vortex Measurements in the Wake of a Hovering Rotor," AHS Paper 01-018, 57th Annual American Helicopter Society Forum, Washington, DC, May 2001.
- ²⁴Martin, P. B., Pugliese, G. J. and Leishman, J. G., "Laser Doppler Velocimetry Uncertainty Analysis For Rotor Blade Tip Vortex Measurements," AIAA CP 2000-0263, 38th Aerospace Sciences Meeting and Exhibit, Reno, NV, 2000. To be published in *AIAA Journal*.
- ²⁵Pugliese, G. J., "Vortex Wake Measurements of a Helicopter Rotor Blade With A Subwing Tip," M.S. Thesis, Aerospace Engineering Dept., University of Maryland, 2001.
- ²⁶Martin, P. B., "Measurements of the Trailing Vortex Formation, Structure, and Evolution in the Wake of a Hovering Rotor," Ph.D. Dissertation, Aerospace Engineering Dept., University of Maryland, 2001.
- ²⁷Leishman, J. G. and Bagai, A., "Challenges in Understanding the Vortex Dynamics of Helicopter Rotor Wakes," *AIAA Journal*, Vol. 36, No. 7, July 1998, pp. 1130-1140.
- ²⁸Clark, D. R. and Leiper, A. C., "The Free Wake Analysis: A Method for the Prediction of Helicopter Rotor Hovering Performance," *Journal of the American Helicopter Society*, Vol. 15, No. 1, 1970, pp. 3-11.
- ²⁹Berenger, T, Favier, D., and Maresca, C., "Experimental and Numerical Investigation of Rotor Aerodynamics in Forward Flight," AIAA Paper 96-0676, 34th Aerospace Sciences Meeting, Jan. 15-18, Reno, NV, 1996.
- ³⁰Kitaplioglu, C., Betzina, M., and Johnson, W., "Blade-Vortex Interaction Noise of an Isolated Full-Scale XV-15 Tilt-Rotor," 56th Annual American Helicopter Society Forum, Virginia Beach, VA, May 2000.
- ³¹Tangler, J. L., "Experimental Investigation of the Subwing Tip and Its Vortex Structure," NASA CR-3058, 1978.
- ³²Barrett, R. V. and Swales, C., "Realisation of the Full Potential of the Laser Doppler Anemometer in the Analysis of Complex Flows," *Aeronautical Journal*, Vol. 102, No. 1016, 1998, pp. 313-320.
- ³³Leishman, J. G., "Seed Particle Dynamics in Tip Vortex Flows," *Journal of Aircraft*, Vol. 33, No. 4, 1996, pp. 823-825.
- ³⁴Iverson, J. D., "Correlation of Turbulent Trailing vortex Decay Data," *Journal of Aircraft*, Vol. 13, No. 5, 1975, pp. 338-342.
- ³⁵McCormick, B. W., Tangler, J. L., and Sherrieb, H. E., "Structure of Trailing Vortices," *Journal of Aircraft*, Vol. 5, No. 3, 1968, pp. 260-267.
- ³⁶Leibovich, S. and Stewartson, K., "A Sufficient Condition for the Instability of Columnar Vortices," *Journal of Fluid Mechanics*, Vol. 126, 1983, pp. 335-356.
- ³⁷Lessen, M. and Paillet, F., "The Stability of a Trailing Line Vortex: Part 2, Viscous Theory," *Journal of Fluid Mechanics*, Vol. 65, 1974, pp. 769-779.
- ³⁸Staufenbiel, R. and Vitting, T., "On Aircraft Wake Properties and Some Methods for Stimulating Decay and Breakdown of Tip Vortices," *Vortex Flow Aerodynamics*, AGARD-CP-494, 1991, pp. 26:1-26:14.
- ³⁹Rule, J. A. and Bliss, D. B., "Prediction of Viscous Trailing Vortex Structure from Basic Loading Parameters," *AIAA Journal*, Vol. 36, No. 2, 1998, pp. 208-218.
- ⁴⁰Brown, C. E., "Aerodynamics of Wake Vortices," *AIAA Journal*, Vol. 11, No. 4, 1973, pp. 531-536.
- ⁴¹Leishman, J. G., *Principles of Helicopter Aerodynamics*, Cambridge University Press, New York, 2000.

Appendix: Blade Parameters and Test Conditions

Radius, R	406.0 mm
Chord, c	44.5 mm
Root cutout, r_o	0.2R
Tip speed, ΩR	89.28 m/s
Airfoil section	NACA 2415
Collective pitch, θ_0	4.5°
Twist, θ_{tw}	0°
Rotational frequency, Ω	30Hz = 70π rad/s
Tip Mach number, M_{tip}	0.26
Tip Reynolds number, Re_{tip}	272,000
Thrust coefficient, C_T	0.0022
Solidity, σ	0.035
Blade loading coefficient, C_T/σ	0.064

Table 1: Parameters of the baseline blade

Radius, R	407.99 mm
Chord, c	44.0 mm
Root cutout, r_o	0.2R
Break point, r_b	0.8R
Sweep, Λ	20°
Tip speed, ΩR	89.72 m/s
Airfoil section	NACA 2415
Collective pitch, θ_0	4.5°
Twist, θ_{tw}	0°
Rotational frequency, Ω	219.9 rad/s
Tip Mach number, M_{tip}	0.3
Tip Reynolds number, Re_{tip}	250,000
Thrust coefficient, C_T	0.00258
Solidity, σ	0.034
Blade loading coefficient, C_T/σ	0.0758

Table 2: Parameters of the swept tip blade

Radius, R	410.00 mm
Root chord, c_o	44.0 mm
Tip chord, c_t	17.6 mm
Effective chord, c_e	37.1 mm
Root cutout, r_o	0.2R
Break point, r_b	0.8R
Taper ratio, τ	0.4
Tip speed, ΩR	91.36 m/s
Airfoil section	NACA 2415
Collective pitch, θ_0	6.0°
Twist, θ_{tw}	0°
Rotational frequency, Ω	219.9 rad/s
Tip Mach number, M_{tip}	0.3
Tip Reynolds number, Re_{tip}	100,000
Thrust coefficient, C_T	0.00259
Solidity, σ_e	0.029
Blade loading coefficient, C_T/σ_e	0.089

Table 3: Parameters of the tapered tip blade

Radius, R	407.0 mm
Chord, c	44.0 mm
Root cutout, r_o	0.2R
Tip speed, ΩR	89.504 m/s
Airfoil section	NACA 2415
Collective pitch, θ_0	4.5°
Twist, θ_{tw}	0°
Rotational frequency, Ω	219.9 rad/s
Tip Mach number, M_{tip}	0.3
Tip Reynolds number, Re_{tip}	250,000
Thrust coefficient, C_T	0.0033
Solidity, σ	0.0344
Blade loading coefficient, C_T/σ	0.0959

Table 4: Parameters of the subwing tip blade